Thatcher, J., Crump, D.A., Devivier, C., Bailey, P.B.S., and Dulieu-Barton, J.M., "Low cost infrared thermography for automated crack monitoring in fatigue testing", Optics and Lasers in Engineering, 126, 2020, 105914. https://doi.org/10.1016/j.optlaseng.2019.105914

Low cost infrared thermography for automated crack monitoring in fatigue testing

J. E. Thatcher[1], D. A. Crump[1], C. Devivier[2], P. B. S. Bailey[3], J. M. Dulieu-Barton[1*].

[1]School of Engineering, University of Southampton, UK
[2]ModExpEng Ltd., Southampton, UK
[3]Instron Dynamic Systems, Instron Division of ITW Ltd., UK
*Janice@soton.ac.uk tel 07776933686

Abstract

The potential of using infrared thermography in the assessment of crack-tip parameters is described. The use of microbolometers is studied specifically to establish their suitability for use in thermoelastic stress analysis (TSA) for establishing the crack-tip parameters and for automatically monitoring crack growth using temperature measurement. To compare the behaviour of the two types of infrared cameras a camera model is devised, which is used to predict the thermoelastic response. A new automatic crack growth monitoring approach is developed based on the temperature measurement from the raw thermal data collected using the microbolometer. The thermoelastic response model and the crack monitoring procedure are demonstrated on 316L stainless steel single edge notch tension (SENT) specimens. Cracks were established in the specimens, grown and monitored using both types of infrared detector. The procedure is validated using measurements from the photon detector and it is shown that accurate stress intensity factors (SIFs) can be obtained from growing cracks using directly the live readings from the microbolometer. The procedure provides a new means for non-contact measurements in fatigue testing, establishing crack growth rate and the SIFs with the potential for actuator control.

Keywords: Infrared thermography; Thermoelastic stress analysis; Crack monitoring; Camera models;

1 Introduction

As cracks evolve in test coupons and structural components during a fatigue test, a typical means of monitoring crack growth is to use the well-established crack opening displacement (COD) gauges [1] [2]. The highly localised and well understood growth of a crack from a notch in a metallic specimen enables the application of a measurement technique, such as the COD gauge. However, the COD gauge needs to be attached to the test specimen and in large structural tests several may be required to monitor crack propagation at multiple sites. In the present paper, an approach is proposed that uses full-field infrared (IR) techniques to monitor and assess the crack propagation by observing behaviour local to the crack tip during fatigue testing. Both passive infrared thermography (IRT) [3] and thermoelastic stress analysis (TSA)

[4] are applied to monitor and assess the crack propagation in single edge notch tensile (SENT) specimens [1]. In contrast to the COD gauge, IRT does not rely on the global behaviour of the test specimen but local measurements at the crack-tip and as it is a full-field technique it can monitor multiple crack progression. IRT has been used successfully in several application areas as a non-destructive evaluation (NDE) technique. Generally, 'active' IRT has been used, which requires additional excitation of the component under evaluation, to generate a change in temperature. The subsequent heat diffusion can be captured using an IR camera and the image sequences are processed to identify defects. The purpose of the present paper is to use IRT as a means of monitoring and assessing crack propagation, whilst the component is under load. Hence, the heat generated as a consequence of the crack progression is used for evaluation, so there is no requirement for an additional thermal excitation source.

TSA is based on the coupling between the elastic deformation of a material and the heat energy developed in a material specimen subject to cyclic loading [5], known as the thermoelastic effect. Figure 1 shows a schematic of the procedure. When a specimen is undergoing cyclic loading in a test machine, the load measurement is recorded from the load cell via an analogue voltage output and the temperature at the crack-tip is recorded by infrared camera in a sequence of images. The IR images captured under cyclic loading are post processed to obtain the 'thermoelastic response' using a 'lock-in' algorithm [6]. The 'thermoelastic response' is essentially a temperature change, ΔT, which is proportional to the stress change in a material and enables the stress redistribution due to crack propagation to be visualised and quantified. The lock-in procedure extracts the mean temperature of the cycle, T_0, the amplitude of ΔT and its phase relative to the applied cyclic load from the IR image sequence by correlating with the load signal in a post process routine. To monitor the crack growth, it would be more desirable to develop a "live" processing technique with little or no post processing, which utilises the full-field IR images shown in Figure 1 as a means for automatic crack monitoring and assessment. A further potential application is the development of a means of actuator control shown as the dotted line in Figure 1.

The overall aim of the present paper is to demonstrate the potential of IRT to monitor and assess crack growth. Therefore, the suitability of using a lower cost FLIR A655SC microbolometer to 'measure' the crack length and using this output to automatically monitor and assess the crack growth is investigated. To validate the findings a FLIR SC5500 photon detector IR camera is used for comparison as photon detectors are traditionally used for TSA [5]. The thermoelastic response from a growing crack is used to establish the protocols

required for an automated monitoring approach prior to the development of the automatic crack growth monitoring procedure.

For the purpose of a more detailed understanding of the behaviour of the two types of IR camera, Section 2 of the paper introduces a novel IR camera model. The model is based on a knowledge of the camera response, in terms of the inherent noise in the camera system, and sensitivity to a given input and allows a quantitative assessment of the thermoelastic response from each detector. For the SENT specimen used in the experiments, the stress distribution ahead of the mode I opening crack is known from linear elastic fracture mechanics [7], allowing a model of the thermoelastic response to be established. The theory underlying the application of TSA to a stationary crack to determine the stress intensity factor (SIF) (K_I) [8] is summarised in Section 3. The results from the TSA model are compared to experimental data generated using the SENT specimen providing an assessment of the feasibility of using the microbolometer for TSA of a growing crack.

In Section 4 of the paper the crack assessment and monitoring procedure is demonstrated using the lock-in post processed IR images from the photon detector (TSA) captured during a constant load controlled waveform fatigue test. In section 5 a stepped, decreasing load waveform is applied to the SENT specimen. The IR response from the microbolometer and photon detector was captured at regular intervals during the fatigue test and was used to obtain the crack length. The novel automatic crack monitoring and assessment procedure is introduced and shown to produce practically identical results to manual approaches and to those obtained from the TSA based approach using the photon detector. The stepped reduction in load represents the desired action to achieve a constant crack growth, i.e. damage evolution control. It is shown that the bolometer can follow the temperature changes accurately, which could provide the basis for a control action by using the temperature change as an input in to the actuator controller.

2 IR camera systems and models

The FLIR SC5500 series photon detector, comprises a 320 x 256 cryogenically cooled Indium Antimonide (InSb) focal plane array (FPA), has a spectral range of 3-5 µm, a noise equivalent temperature difference (NEDT) of 0.02 K and an integration time (electronic shutter speed) adjustable between 3 µs to 20ms with a maximum frame rate of 383 Hz when using the entire detector array; faster frame rates can be achieved by using fewer detectors in the array (i.e. windowing). The voltage output from the detector essentially allows the photons to be counted and converted to a digital signal in digital level (DL), which are converted to temperature using

an inbuilt calibration. The FLIR A655SC microbolometer IR camera has a vanadium oxide (VoX) UFPA detector, a spectral range of 7.5–14 μm, and a resolution of 640 x 480 pixels. The thermal time constant is described as typically less than 8 ms and the NETD as less than 30 mK. The maximum recording frequency is 50 Hz. As the temperature increases, the resistance of the detector decreases. The resulting voltage change is converted to DL and then temperature using an inbuilt calibration. The cameras also have different dynamic ranges as the analogue to digital convertors (ADC) incorporated in each system have different resolutions. The microbolometer has a 16 bit ADC, giving a dynamic range of 65536 DL, and the photon detector has a 14 bit ADC, with dynamic range 16384 DL.

In the experiments described in this section only the camera DL was recorded to negate any effect of the temperature calibration procedure. It should be noted that as the devices are different, working in a different wavelength window, temperature range, and the microbolometer measures radiance, whereas the photon detector counts photons, the DL values for the microbolometer and the photon detector are not directly comparable. Planck's law for radiance (R) from a perfect emitter or blackbody over the microbolometer detector operating wavelengths is:

$$R = \int_{7500}^{14000} \frac{2hc^2\lambda^{-5}}{e^{\frac{hc}{k\lambda T}} - 1} d\lambda \tag{1}$$

and for the photon detector the photon count, PC, [9] is:

$$PC = \int_{2500}^{5100} \frac{2hc\lambda^{-4}}{e^{\frac{hc}{k\lambda T}} - 1} d\lambda \tag{2}$$

where h is Planck's constant, c is the speed of light, λ is the wavelength, k is Boltzmann constant, and T is temperature.

To fully understand the performance of each system, a camera modelling approach was developed based on the camera performance over a range of temperatures. To produce the camera model the response of the camera to a given thermal input, i.e. its sensitivity, and the inherent variation in the response, i.e. noise content, must be established. To derive the sensitivity and the noise content experimentally it is necessary to use a temperature controlled black body, to generate a variety of temperatures, so that the camera response can be recorded in DL.

The black body used was an Infrared Systems Development Corporation, IR-2106/301 plate source, with a temperature range of 5 to 150 °C, a wavelength range of 1 to 99 μm, and an

emissivity of 0.96 +/- 0.02. The emitter size is 152 mm x 152 mm, has a temperature resolution of 0.1 °C and a temperature stability of +/- 0.1 °C short term and +/- 0.2 °C long term; its emissivity is quoted as >0.95 over the wavelength range 0.8 to 30 μm. Temperature control is maintained by an IR-301 P.I.D controller. Table 1 shows the temperatures and frame rates used in the tests; a constant integration time of 500 μs was used for the photon detector to facilitate measurement over a wider range of frame rates and temperatures. The temperatures chosen are typical of those observed during typical crack propagation tests. Fewer frames were recorded for the microbolometer, because of the slower frame rates that can be achieved, and the possibility of crack growth during the actual experiments on the SENT specimen; hence the photon detector recorded 1000 frames during each test and the microbolometer 100 frames in each test. The frame size for the photon detector was reduced from 320 x 256 to 160 x 128 to facilitate data collection over a wider range of frame rates in excess of the maximum 383 Hz achievable at full frame. The stand-off distance was about 30 cm, so practically all the blackbody plate could be viewed and the set-up was shielded from external heat sources using a shroud.

Table 1. Experimental parameters used for camera performance assessment.

	Frame size (Pixels)	No. of frames recorded	Test temps (°C)	Frame rate (Hz)	Integration time (μs)
SC5500	160 x 128	1000	15, 20, 40, 50, 60, 70	25, 100, 200, 500, 1000, 1253	500
A655SC	640 x 240	100	15, 20, 30, 40, 50, 60, 70	3.13, 6.25, 12.5, 25, 50	NA

The detector non-uniformity correction (NUC) was not applied to avoid modifying the noise content, as the NUC procedure scales values and therefore also scales the noise. Therefore, the recorded images contained a non-uniform pattern associated with the detector architecture. To remove the non-uniform pattern, the temporal mean was established for each element in the detector array over the image sequence. The mean was then subtracted from the response of each element in the detector array in each frame of the image sequences. The noise content was established by deriving the standard deviation (*STD*) of the response in the recorded image sequence for each black body temperature and each frame rate as follows:

$$STD = \sqrt{\frac{1}{NX}\frac{1}{NY}\frac{1}{NF}\sum_{x=1}^{NX}\sum_{y=1}^{NY}\sum_{i=1}^{NF}\left(img\left(x,y,i\right)-\frac{1}{NF}\sum_{j=1}^{NF}img(x,y,i)\right)^2} \quad (3)$$

where *NX* is the detector number in the horizontal direction, *NY* the detector number in the vertical direction, *NF* the number of recorded frames and *img*(*x,y,i*) is the image sequence recorded at one temperature and one frame rate.

The sensitivity was established by using the mean of the recorded images versus *R* or *PC* (depending on the detector type). The temperature of the black body was used in equations (1) and (2) to calculate *R* and *PC* respectively. The mean, *MEAN*, is derived using the following expression:

$$MEAN = \frac{1}{NX}\frac{1}{NY}\frac{1}{NF}\sum_{x=1}^{NX}\sum_{y=1}^{NY}\sum_{i=1}^{NF}img\left(x,y,i\right) \quad (4)$$

Figure 2 is a plot of the *STD* against the *MEAN,* indicating the inherent noise content in each camera response. It can be seen from the plots in Figure 2 that the microbolometer noise content does not vary with the mean value, whereas the noise produced by the photon detector increases with the mean DL value. However, the linear correlation coefficient for each frame rate is much less than 1 for the microbolometer, indicating that there is significant data scatter. The reason the inherent noise scales with the input temperature for the photon detector is because there is quantum noise associated with the conversion of the impinging photons into electrons; the greater the temperature input the greater the photons, for any given integration time. Conversely, the microbolometer heats according to the input temperature, so the noise must emanate from the read-out circuit and hence is independent of the input temperature. For both the photon detector and microbolometer there is a general trend of higher noise at the lower frame rates where the image capture duration is up to 40 seconds. Therefore, the increase in noise can be attributed to the stability of the blackbody temperature, i.e. 0.1 °C. Figure 3 is a plot of the *MEAN* against the response derived from both cameras at every temperature and every frame rate given in Table 1, indicating the sensitivity. Figure 3 shows that, as expected, both cameras respond linearly to increasing input and importantly, in contrast to the inherent noise, the response is independent of frame rate. In Figures 2 and 3, for the photon detector at the largest mean DL value, there is an outlier showing a low noise and low response, this is because at this temperature the detector has saturated.

The overall detector noise content and sensitivity were obtained from the linear fits plotted in Figures 2 and 3, respectively, for each frame rate. From the linear fits the overall slope and intercept for all recording conditions, were determined along with the linear correlation

coefficient and are given in Table 2. A correlation coefficient is not reported for the microbolometer noise equation in Table 2 as there was little correlation (see Figure 2) and hence the maximum noise value is used as the intercept value reported in Table 2. The generated linear expressions from Table 2 were integrated into a Matlab script to obtain the detector models. In interpreting the values in Table 2 it is important to emphasise that the DL values for each camera are not the same and hence a comparison cannot be made regarding performance. Therefore, in assessing the suitability of camera system for TSA it is necessary to model an identical input in to each camera; this is done for the particular case of the SENT specimen in section 3. However, what can be inferred from Table 2 is that regardless of the input temperature the noise performance of the bolometer will be constant, as long as the temperature measured is above the minimum resolvable temperature for the system.

Table 2. Noise and sensitivity equations for the microbolometer and photon detector.

	Noise			Sensitivity		
	Slope	Intercept (DL)	Correlation coefficient	Slope	Intercept (DL)	Correlation coefficient
Microbolometer	0	21.4	N/A	167.9 DL/R	4282.7	0.999
Photon detector	3.0×10^{-4}	2.1	0.602	1.4×10^{-17} DL/PC	981.1	0.999

3 Detector model of thermoelastic response

The two detector models were used as the basis to develop a model of the thermoelastic response from each camera system. The model of the thermoelastic response is based on a stationary crack developed in the SENT specimen after 82,000 cycles, with a total crack length of 17.80 mm. This crack length was chosen because the crack growth was well established. Figure 4 shows the overall dimensions of the SENT specimens used throughout the work described in the paper. The specimen material was chosen as 316L stainless steel as it has well understood material and thermoelastic properties [10] [11] and the fine grain structure ensures a consistent crack growth. The specimen was coated with a thin layer of RS matt black paint with emissivity given as around 0.92 [10]. The TSA data was obtained when the cracked SENT specimen was subjected to a load of 11.55 kN, with an amplitude of 5 kN and a frequency of 10 Hz, which gave a K_I value of 34.78 MPa.m$^{1/2}$, ensuring that during the data collection the crack was stationary.

The insert in Figure 4 shows the coordinate system used in this work; the origin is the crack tip. In fracture mechanics polar coordinates, (r, θ) are used to derive the crack-tip parameters. As the thermal images are essentially made up from a grid of responses from the individual sensors in the detector array the analysis lends itself to a Cartesian coordinate system, i.e. pixel by pixel, which is also shown in Figure 4.

The starting point in the analysis is to combine the well-known expression for the thermoelastic response [5] with that for the mode I SIF based on the Westergaard equations [8]. The approach for deriving the mode I SIF from thermoelastic data was described in [8], and is applicable for an isolated crack in the centre of a large plate, where $K_I = \sigma (\pi a)^{1/2}$. It is this approach that is used in the present paper so only the key steps in defining the thermoelastic model are provided. The thermoelastic response is related to the mode I SIF, K_I, as follows:

$$\frac{\Delta T}{T_0} = \frac{2KK_I}{\sqrt{2\pi r}}\cos\left(\frac{\theta}{2}\right) \tag{5}$$

where ΔT is the small temperature change caused by the thermoelastic effect [4], K is the thermoelastic constant (obtained experimentally as 4.73 x 10^{-6} MPa^{-1}, see below - equation (12)) and T_0 is the absolute mean temperature of the specimen during the cyclic loading.

To generate the model the origin (the crack-tip) was defined in Cartesian coordinates (see Figure 4) in the model image frame. The location of the response for each image pixel relative to the crack-tip was then defined as follows:

$$r = \sqrt{(x - x_{CT})^2 + (y - y_{CT})^2} \tag{6}$$

$$\theta = tan^{-1}\frac{y - y_{CT}}{x - x_{CT}} \tag{7}$$

where the subscript CT indicates the coordinates of the crack tip.

Equation (5) is used to generate ΔT pixel by pixel for each image frame corresponding to the sensor array size for the bolometer and the photon detector to give $\Delta T(x,y)$. T_0 is set to 293 K, allowing a cyclic variation of temperature, $T(x,y,t)$, to be generated as follows:

$$T(x,y,t) = T_0 + 0.5\Delta T(x,y)\cos(2\pi f_0 t + \phi) \tag{8}$$

where t is time, f_0 is the specimen loading frequency. Φ is the phase of ΔT with respect to the stress change, which is set to π for the purposes of producing the model.

100 images are generated for the bolometer and 1000 for the photon detector at the appropriate frames rates corresponding to the actual image capture during the experiment to give $T(x,y,t)$. The next step in the procedure is to convert $T(x,y,t)$ into R for the microbolometer and PC for the photon detector, using equations (1) and (2) respectively. The appropriate noise and sensitivity expressions for both the bolometer and the photon detector are then applied to each image frame of simulated data to produce an image sequence that models the thermal images that would be collected, by each detector, during cyclic loading expressed in terms of DL. The final step is to extract the TSA data T, ΔT and Φ, from $T(x,y,t)$ in DL. This was done by applying a nonlinear optimisation using a cost function of the RMS error between $T(x,y,t)$ and values computed using equation (8) on each pixel in each frame of the image sequence. It should be noted that as the surface emissivity of the black body, used to collect the data to construct the model, is slightly greater (by approximately 0.03 to 0.04) than the matt black paint used in the experiments the response given by the models should be greater than that of the experiment.

A comparison of the ΔT experimental and simulated results for the microbolometer is shown in Figure 5. The experimental data shows the typical cardioid shape expected in the region of the crack tip [12]. However, the modelled ΔT values are approximately 2.5 times larger than the experimental results. This is because the microbolometer is not able to respond adequately to the rapid temperature changes occurring in the experiment and acts effectively as a low pass filter [13] [14]. The microbolometer is limited in its response by its thermal time constant which is fixed and is based on the sensor material and architecture; for the FLIR A655SC this is 8 ms and the response time is much longer [15]. The overall filtering effect is shown in Figure 6 where a plot of the raw temperature data from a single pixel is shown against time. The reconstructed thermoelastic response is also shown in the plot, which is sinusoidal with a frequency of 10 Hz, and a T_0 of around room temperature (which is correct). However, ΔT is much smaller than the expected value of 0.65 K because of the detector response time.

It has been shown that accurate ΔT values can be obtained through a calibration procedure that accounts for the reduction in the response at each loading frequency [13], but this requires additional processing. Figure 7 shows experimental ΔT plots from the microbolometer and from the photon detector, in Kelvin, after the calibration procedure has been applied to the microbolometer data; there is a reasonable qualitative correspondence. However, it is evident that the effect of rigid body motion, which has not been corrected for in the bolometer data, is smearing the response and is particularly noticeable around the machined notch. An estimate of the motion local to the notch, which is 7 mm in length, can be provided by scaling the image and is about 1 mm. Therefore, the distorted image from the bolometer, alongside the additional

noise, can be attributed to the motion. The motion can be corrected for by additional processing of the thermal images using image correlation approaches, e.g. [16], but is not done here as the object of the paper is demonstrate the raw thermal data can be used directly to monitor and assess the crack growth. Another reason for the difference may be attributed to the lack of an analogue voltage input to the Flir A655SC microbolometer and hence the necessity to use the approximated loading frequency from the test machine display. Additionally, as it is not possible to simultaneously record the load cell output (see Figure 1) for the lock in, it was necessary to simulate the phase of the response. This was achieved by first creating a simulated "lock in" signal at the loading frequency measured from the test machine, then the phase value that occurred most frequently in the photon detector data was used to adjust the bolometer phase value to match.

A qualitative visual assessment of the photon detector model in Figure 8, shows that there is a stress concentration at the crack-tip but response is much smaller (note the different scale); this is because the model is constructed using data captured with a shorter integration time, than used in the experiment. Therefore, another model was produced by collecting data from the black body at the same integration time as the experiment of 1332 µs. The black body temperature was restricted because of saturation of the detector, so only 3 temperatures were used in the model, but 5 frame rates were used. The resulting model output is shown in Figure 8 and clearly corresponds very well to the experimental data. However, some key important differences highlight the deficiencies in using the Westergaard equations to fit the thermoelastic response, which only consider linear elastic behaviour and assume a centrally placed crack in a thin infinite plate. To highlight these differences and additional plot is provided in Figure 8, which shows a difference map of the experimental data subtracted from the model data. There is a large negative difference close to the crack tip because of the heat generated as a consequence of plasticity. Away from the crack, in the region of more uniform stress that is unaffected by heat transfer from the plastic zone, the thermoelastic response predicted by the model is slightly greater than that of the experiment. This is because the emissivity of the black body used to generate the model data, is greater than that of the matt black paint used to coat the test specimen.

To make a quantitative comparison of the noise in the experimental data with that of the model for the TSA processing an area to the top right of each image in Figures 5 and 8 was analysed. The area was 30 x 30 pixels in size and in a region of more uniform stress away from the influence of the crack tip. Table 3 gives the mean, standard deviation and coefficient of variation of the thermoelastic response for the model and experimental data for both the microbolometer and the photon detector in DL. Accepting the response over the region may

vary slightly, due to the stress gradient across the region, the results demonstrate clearly how the TSA processing facilitates the identification of the very small thermoelastic temperature change. The mean TSA values given in Table 3 are well below the noise threshold value of both the detector types, as provided in Figure 2. However, it should be considered that the T_0 (see equation (8)) values are of the order 13000 DL for the bolometer and 5000 DL for the photon detector, which are well above the noise threshold for both cameras. For the microbolometer the model and the experimental TSA mean and standard deviation values are not comparable due to the response time of the detector not being accounted for in the TSA processing (as discussed above). However, the coefficient of variation shows that the experimental data contains more noise than the model. This is expected because of motion and because of surface irregularities in the experiment. The same is seen in the photon detector data but here the coefficient of variation is much lower with about 7% noise compared to 24% noise for the microbolometer. Interestingly, the models for the photon detector show that the noise scales linearly with input (see Figure 2) and is reflected in the TSA processing with the increased integration time having no effect on the noise content of the response.

Table 3. Resolution of TSA analysis for the microbolometer and the photon detector.

	Microbolometer		Photon Detector		
	Experiment	Model	Experiment	Model 500 μs	Model 1332 μs
Mean (DL)	4.328	15.841	20.158	8.350	21.472
Standard deviation (DL)	1.049	2.878	1.448	0.327	0.638
Coefficient of variation (%)	24.2	18.2	7.2	3.9	3.0

The modelling approach has demonstrated clearly that although microbolometers have been used successfully in TSA studies of material behaviour and crack growth, e.g. [17] [18], their use requires significant image and signal processing. Factors to consider include the loading frequency calibration and any motion correction both of which require further processing, and they do not readily have the inbuilt capacity to read in the a signal from the load cell to perform the lock-in. Hence, in the following sections the thermal images captured by the photon detector are processed in to TSA data and then are used to provide validation of the automated crack assessment and monitoring procedure implemented using only raw thermal data from the microbolometer.

4 Assessing and monitoring crack growth using TSA

The diagram in Figure 1 indicates that the raw thermal images require significant processing to extract T_0, ΔT and Φ (see equation 8). There is a substantial body of successful work dating back to papers by Stanley and his co-workers in the 1980s [8], e.g. [12] [19] [20] [21] [22] [23],

where SIFs are extracted from the thermoelastic response. However, adopting these procedures for monitoring the crack progression would be inefficient due to the post processing that is required in addition to simply deriving ΔT from the thermal images. Work has been conducted on using the thermoelastic phase data to establish the position of the crack tip and derive the SIF [24] [25] but also requires the additional post processing. Here, the proposal is to use T_0 to establish the crack-tip location and determine the crack advance. The aim is to demonstrate that the crack propagation can be monitored using a temperature measurement alone, using T_0 as an analogue for the raw temperature data taken directly from thermal images as a first step, because T_0 is extracted from a long image series collected for TSA the effect of noise is minimised. Therefore, in the preliminary tests to determine the suitability of using IR techniques for crack growth monitoring, only the FLIR SC5500 series photon detector was used. To provide a route for validation, TSA post processing was applied to give not only T_0, but ΔT and Φ as well. If the position of the crack tip can be identified using this data then the crack length can be established, so K_I can be obtained as follows [1]:

$$K_I = C\sigma\sqrt{\pi a} \tag{9}$$

where σ is the applied stress in the specimen section away from the crack and a is the total crack length (including the initial notch which in all cases was 7mm long- see Figure 4) and C is the SIF geometry function [7]:

$$C = 1.12 - 0.2318\left(\frac{a}{W}\right) + 10.55\left(\frac{a}{W}\right)^2 - 21.72\left(\frac{a}{W}\right)^3 + 30.39\left(\frac{a}{W}\right)^4 \tag{10}$$

where W is the specimen width.

By plotting the crack growth rate (da/dN) and the temperature evolution rate (dT/dN), against ΔK_I, it can be determined if the temperature evolutions follow the Paris law. The x and y coordinates of the maximum T_0 can be identified in the TSA data and used with the known applied stress to give K_I. The location of the crack tip relative to the end of the notch in the SENT specimen is given in pixels; this is converted to metres, to give a in equation (9) using the known notch length. Additionally, as a means of validation, ΔT can be used to provide K_I [8] as follows:

$$K_I = C\sqrt{\frac{4\pi m}{3\sqrt{3}K^2}} \tag{11}$$

where m is the gradient of a plot of $1/(\Delta T/T_0)^2_{max}$, against the y coordinate.

A SENT specimen was cyclically fatigued in load control at a constant load amplitude. The specimen was subjected to a mean load of 11.55 kN and an amplitude of +/- 9.45 kN at a frequency of 10 Hz, giving an R value of 0.1. The test specimen was tested continuously to

failure. T_0, ΔT and Φ were obtained by applying TSA to an images series of 1000 frames captured every 1000 cycles; the photon detector frame rate was 383 Hz, with an integration time of 1332 µs.

In the wake of the crack tip 'hotspots' develop due to frictional heating as the crack faces rub together. Away from the vicinity of the crack tip, additional spurious hot spots may occur as a result of, e.g., reflections. To eliminate these hotspots from the analysis, a region of interest was defined as a maximum of five horizontal pixel rows either side of the crack tip, and ahead of the crack tip. In Figure 9, three horizontal T_0 profiles are shown taken from three adjacent horizontal lines of pixels from the edge of the specimen. Overlaid on the T_0 plots in Figure 9 is a plot of the phase values taken along the crack line. It is clear that to the left of the sharp change in the phase the noisy T_0 values occur because of the crack face rubbing. It should be noted that the sharp change in phase is an artefact of plotting the phase values between -180^o and +180^o. The plastic region at the crack tip causes localised heating and heat transfer. To the right of the sharp change in phase the region affected by the plasticity is identified between 16.5 and 18.5 mm, after which the phase returns to a constant value. It is clear that attempting to identify the crack tip using the phase data is open to interpretation, in Figure 9 this could be located according to the phase anywhere between 16.5 and 18.5 mm. Therefore, only the maximum value of T_0 is used in the following analysis to locate crack tip. Furthermore, without the TSA processing only the maximum temperature value could be used to monitor the crack propagation.

To derive K_I from the thermoelastic data and provide additional validation, $1/(\Delta T/T_0)^2_{max}$, must be plotted against the y coordinate of each horizontal line in the ΔT image [8]. A Matlab script was developed to extract the gradient of the plot from each image series captured as the crack advances. As equation (11) was developed from the Westergaard equations and linear elastic fracture mechanics the script only considers data between 0.5 mm and 4 mm away from the crack tip (i.e. r << a).

The thermoelastic constant, K, was calculated using an average value of $\Delta T/T_0$ away from the region of the crack and the nominal applied stress range, $\Delta\sigma$:

$$K = \frac{\Delta T}{T_0 \Delta \sigma} \tag{12}$$

The crack length determined from maximum T_0 and ΔT were used to calculate K_I. Figure 10 plots the evolution of K_I with cycle count using the crack length and equation (11). The TSA

data is given in two forms, with and without the geometry correction given in equation (10). It is evident that the geometry correction is required as this results in a good correlation between the SIFs calculated from the location of the maximum T_0 and the SIFs calculated using equation (11). As the crack advances the difference in the SIFs calculated by two technique increases with the equation (11) giving slightly larger values. Figure 10 validates that the crack length determined using a temperature measure alone can provide the necessary information to determine SIFs.

To investigate if the temperature measurement is related directly to the SIF, Figure 11 plots the crack propagation rate, *da/dN*, and temperature evolution rate, dT_0/dN, against the change in stress intensity factor, ΔK_I, for the constant load test. Linear trend lines for both datasets are also included, with their corresponding equations. The trend line equations give the Paris law parameters axis intercept point and gradient from the *da/dN* plot as 1.50×10^{-7} m/cycle and 1.28×10^{-7} $m^{1/2}$/MPa cycle respectively and from the *dT/dN* plot as -1.11×10^{-4} ^{o}C/cycle and 2.59×10^{-4} ^{o}C/MPa $m^{1/2}$ cycle respectively. Although the 'Paris parameters' are different, it is encouraging to note that the rate of temperature evolution is linear and follows the same trend as the measured crack propagation. This strongly indicates that crack growth can be monitored using the temperature directly measured at the crack tip instead of monitoring the crack tip location. Moreover, comparison of the two gradient indicates the temperature provides a very sensitive measure of crack growth (in 316L stainless steel) of approximately 0.5 mm/^{o}C, albeit using very sparse data. Another important observation from Figure 11 is the lack of data at the end of the test, where the rapidly growing crack leads to a change in ΔK_I of 8.013 to 26.096 across three data points. This identifies the need to control the crack propagation so that more data points can be obtained from the end of the test. The next step is to demonstrate that the bolometer alone can automatically detect the crack advance accurately using raw temperature data obtained directly from the camera output.

6 Using the microbolometer for automatic monitoring of crack growth

For the purposes of validation, both types of IR detector were positioned so that each side of a SENT specimen was viewed simultaneously. The photon detector had its recording parameters set identically to that described in the previous section; the bolometer was set to record at a frame rate of 50 Hz. The stand-off distance was such that the spatial resolution for the photon detector images was 0.132 mm/pixel and 0.2 mm/pixel for the microbolometer images. To enable more data points to be collected towards the end of the test and to establish the sensitivity of the technique to changing crack-tip stresses the test was controlled to provide a constant crack growth rate based on the results from the previous section. The target was

to provide a linear increase in K_I, so the SENT specimen was cyclically loaded with a stepped decreasing load amplitude. The specimen was initially subjected to a mean load of 11.55 kN and an amplitude of +/- 9.45 kN, giving an initial R value of 0.1, and at a frequency of 10 Hz. The loading frequency remained constant throughout the test, and the R value reduced.

The point at which the load amplitude was reduced was when the test machine read-out showed the maximum displacement had increased by 0.01 mm, as in the constant load amplitude test described in the previous section 0.01 mm was the displacement where the temperature started to increase more rapidly (see Figure 12). The test machine controller was set to reduce the load amplitude when the maximum displacement increased to 0.01; the mean load and frequency were maintained, and the test continued without interruption. After 100 cycles at the lower amplitude, a new reference maximum displacement was recorded. The displacement was monitored until another 0.01 mm increase from the new reference value was recorded, then a further reduction in load amplitude was applied. The process was repeated four times before the test was stopped. Table 4 shows the mean load and different load amplitude applied during the tests, and the cycle numbers when each were applied.

Table 4. Loads for controlled crack growth test.

Cycles	0 - 26380	26381 - 48184	48185 - 63967	63968 - 82537	82538 - 101459
Mean Load	11.55kN	11.55kN	11.55kN	11.55kN	11.55kN
Amplitude	9.45	8.00	6.50	5.00	4.00

The crack tip monitoring techniques used with the photon detector were repeated for this test. For the microbolometer, the embedded ResearchIR software was used to identify the maximum temperature within a user defined region of interest and the related *x* and *y* pixel coordinates for each image in the temporal sequence. The temporal sequence of maximum temperatures, and coordinates, was inspected to find the highest value. The coordinates of the highest maximum temperature within the sequence was defined as the crack tip location.

To automate the process an automatic crack tip detection and tracking algorithm was implemented in Matlab and applied to the image sequences collected from the microbolometer as the crack progressed. The crack tip position was established by locating the maximum difference in temperature at each pixel over the 100 images in each sequence. To identify the maximum temperature difference the temporal minimum is subtracted from the temporal maximum of the recorded images at each pixel. A temporal mean is established for each pixel which is used to create the mean matrix, by averaging all the recorded images with time. The detection matrix is obtained by dividing each value of the range matrix by the corresponding

value in the mean matrix. The crack tip location is at the maximum value of the detection matrix.

To start the process, only *a-priori* knowledge of an approximate crack propagation direction is required. For the very first set of recorded images, the crack tip location is unknown and a manual selection process has to be followed, which in the SENT specimen is easily identifiable because of the starter notch. For the following sets of recorded images, the search window is positioned such that the only the part of the matrix that is in front of the crack tip along the propagation direction could be used to identify the crack tip location. This search window follows the last found crack tip location. As the data processing time is short, around 5 seconds, the crack tracking can be carried out on image sequences as they are captured, and a live readout is produced of the crack advance in the image frame alongside a calculation of K_I, which is also output as a live display. Moreover, a threshold can be set for K_I so that when this is exceeded a command signal could be sent to the actuator controller. For the case of the SENT specimen there is an analytical solution for K_I, as is the case for several other standard test specimens, which are provided in the literature, e.g. [7]. It would be a straightforward proposition to implement these into the crack tracking algorithm. For a general structure, these are not available, but it would still be possible to track the crack tip location, and use approximations to establish K_I; this is the object of further work in particular application to composite materials.

Figure 13 plots the evolution of the maximum temperature, from both the photon detector T_0 and microbolometer T, and the maximum and minimum actuator displacement with cycle count. The maximum actuator displacement line clearly shows the progress of the crack opening and the effect of the load reductions. It can be seen that there is a small acceleration in the temperature change rate, measured by both the photon detector and microbolometer, just before each load reduction, indicating that the crack growth could be controlled by using an increase in the gradient of the temperature change to trigger an actuator control action. There is also a drop in temperature just after the decrease in the load amplitude which is expected due to the resulting reduced crack-tip stresses and plasticity. Whilst the microbolometer temperature follows the general trend of photon detector, as predicted by the model there is more noise, resulting from the lower sensitivity and also the effects of motion, but also because the data has not been processed by the lock-in. In the first load step, it can be seen that there is a small difference between the photon detector T_0 and the maximum temperature extracted from the microbolometer. This can be attributed to the larger motion experienced in the first load step, which is compensated for only in the photon detector data. As the load is reduced to control the crack propagation there is less energy dissipated as heat

at the crack tip and hence identifying clear changes in temperature becomes more difficult. This is clear in the final load step in Figure 13 where the scatter in the response from the microbolometer is greater than the temperature increase over the loading step. A comparison of the manual and automated crack monitoring approach using the raw thermal data shows that both provide virtually identical results, which demonstrates that effectiveness of the automated procedure.

In Figure 14 the evolution of K_I against cycle count is plotted. K_I is derived using the crack length derived from the maximum temperature using Equation (11); i.e. T_0 for the photon detector and T for the bolometer using both the manual and automatic monitoring procedure. Figure 14a shows the evolution of ΔK_I and Figure 14b shows for comparison the evolution of K_{Imax}. As expected, the reduction in the load causes a reduction in ΔK_I, which then increases as the crack propagates. For K_{Imax} the increase is constant demonstrating the potential to adopt such an approach for actuator control. It is very clear that the K_I values obtained from each temperature measurement correspond practically exactly to each other and demonstrates that the microbolometer can be used as a simple automatic non-contact crack tracking device despite the increased noise in the thermal data. The reason for this is because the crack tracking algorithm is not dependent on the absolute value of T_{max} but only its location. It should be noted that the sharp reduction in K_I and the plateauing of the crack growth rate is primarily due to the coarse control of the test machine. Figure 15 shows the final image with the automatically derived crack path overlaid. It is clear from the image that there is some localised heating occurring at the start of the crack which could be attributed to frictional effects. However the hot spot at the crack tip is clear and it is evident that tracking the hot spot closely follows the crack propagation.

7 Conclusions

It has been demonstrated that a camera model can be developed that incorporates the inherent camera noise and sensitivity and used to evaluate the performance of IR detectors when used for TSA. The models revealed that careful selection of the integration time is required when using the photon detector. However, the bolometer did not produce the expected thermoelastic response predicted by the model, because of the fixed response time of the system, which is dependent on the detector material. As the bolometer simply acts as a low pass filter on the cyclic temperature data it is possible to conduct a linear calibration to obtain the correct thermoelastic response. However, using TSA as a basis for directly monitoring the crack propagation using the low cost microbolometer was discounted because of the extra processing required on the thermal data. Instead a procedure has been developed

and demonstrated that utilises directly the unprocessed output from the microbolometer in an automated approach.

A SENT specimen subjected to a constant amplitude load was used to evaluate the feasibility of using mean temperature measurement to derive SIFs. The feasibility was demonstrated using photon detector and lock-in processing to provide a mean temperature value over 1000 images, which was used to determine the crack length. It was shown that this approach could provide SIFs to the same level of accuracy as a well-established approach based on the thermoelastic response.

The effectiveness of the microbolometer for tracking the crack-tip was then evaluated using the approach developed using the photon detector. It was shown that the raw thermal data from 100 frames could be used to determine the crack length. An automatic crack tip tracking procedure was developed that was shown to be equally effective as the manual procedure and can be carried out live as the crack progresses.

In summary:

- Both the photon detector and microbolometer were able to detect and monitor crack growth.
- The SIF derived directly from the thermoelastic response correlated virtually exactly with the SIF's obtained from the crack length measurements.
- The temperature increase rate correlated well with the Paris crack growth law.

The work described in the paper has demonstrated infrared techniques can be used to monitor crack growth. Moreover, low-cost microbolometers have been shown to be as effective as photon detectors for monitoring crack progression by utilising raw temperature data rather than using TSA processing to evaluate the SIFs. Furthermore, the automated crack tracking approach to evaluate the SIFs is independent of loading frequency and material, which need to be considered when applying TSA to evaluate the SIFs. It may also be concluded that if the microbolometer could be incorporated into an actuator control system then its output could be used directly to control the actuator displacement. The low cost of microbolometers means that many cameras could be used in large structural tests both for crack monitoring and actuator control, which will be the object of future work.

Acknowledgements

The authors thank Instron Division of ITW Ltd., UK and the EPSRC for funding the research. The experimental work described in the paper was conducted in the Testing and Structures Research Laboratory (TSRL) at the University of Southampton https://www.southampton.ac.uk/engineering/research/facilities/360/tsrl_360.page. The authors are grateful for the support received from Dr Andy Robinson, the TSRL Principal Experimental Officer.

References

[1] British Standards, "BS ISO 12108 Metallic Materials. Fatigue testing. Fatigue crack growth method", 2012.

[2] ASTM international, "ASTM E647-13ae1 Standard Test Method for Measurement of Fatigue Crack Growth Rates".

[3] J. Fan, X. Guo and C. Wu, "A new application of the infrared thermography for fatigue evaluation and damage assessment", *International Journal of Fatigue,* vol. 44, pp. 1-7, 2012.

[4] P. Stanley and W. K. Chan, "Quantitative stress analysis by means of the thermoelastic effect.", *Journal of Strain Analysis,* vol. 20, no. 3, pp. 129-137, 1984.

[5] J. M. Dulieu-Barton, "Thermoelastic stress analysis", in *Optical Methods of Solid Mechanics*, Weinheim, Wiley-VCH, 2012, pp. 345-366.

[6] G. Pitarresi, L. D'Acquisto and A. M. Siddiolo, "Thermoelastic stress analysis by means of an infrared scanner and a two-dimensional fast Fourier transform based lock-in technique", *Journal of Strain Analysis,* vol. 43, pp. 493-506, 2008.

[7] H. L. Ewalds and R. J. H. Wanhill, Fracture Mechanics, London: Edward Arnold, 1986.

[8] P. Stanley and W. K. Chan, "The determination of stress intensity factors and crack tip velocities from thermoelastic infra-red emissions", *Proc. of International Conference on Fatigue of Engineering Materials and Structures,* vol. C262, pp. 105-114, 1986.

[9] J. A. Jamieson, R. H. McFee, G. N. Plass, R. H. Grube and R. G. Richards, Infrared Physics and Engineering, McGraw-Hill, 1963.

[10] A. F. Robinson, J. M. Dulieu-Barton, S. Quinn and R. L. Burguete, "Paint coating characterization for thermoelastic stress analysis of metallic materials", *Measurement Science and Technology,* vol. 21, 2010.

[11] L. Bodelot, L. Sabatier, E. Charkaluk and P. Dufrenoy, "Experimental setup for fully coupled kinematic and thermal measurements at the microstructure scale on an AISI 316L steel", *Materials Science and engineering: A,* vol. 501, no. 1, pp. 52-60, 2009.

[12] P. Stanley and J. M. Dulieu-Smith, "The detemination of crack-tip parameters from thermoelastic data", *Experimental techniques,* vol. 20, no. 2, pp. 21-23, 1996.

[13] I. Jimenez-Fortunato, D. J. Bull, J. M. Dulieu-Barton and O. T. Thomsen, "Towards integrating imaging techniques to assess manufacturing features and in-service damage in composite components", in *SEM Annual Conference*, Greenville, 2018.

[14] N. Rajic and D. Rowlands, "Thermoelastic stress analysis with a compact low-cost microbolometer system", *Quantitative Infrared Thermography Journal,* vol. 10, no. 2, pp. 135-158, 2013.

[15] H. Budzier, V. Krause, S. Bohmer, G. Gerlach and U. Hoffmann, "Fast microbolometer based infrared camera system", DIAS Infrared GmbH-Publications-No 20.

[16] W. Wang, R. K. Fruehmann and J. M. Dulieu-Barton, "Application of digital image correlation to address complex motions in thermoelastic stress analysis", *Strain,* vol. 51, pp. 405-418, 2015.

[17] R. B. Vieira, G. L. Gonzales and J. L. Freire, "Thermography applied to the study of fatigue crack propagation in polycarbonate", *Experimental Mechanics,* 2017.

[18] A. K. Wong, N. Rajic and Q. Nguyen, "50th Anniversary article: seeing stresses through the thermoelastic lens-A retrospective and prospective from an Australian viewpoint", *Strain,* vol. 51, pp. 1-15, 2015.

[19] R. A. Tomlinson and E. J. Olden, "Thermoelasticity for the analysis of crack tip stress field", *Strain,* no. May, pp. 49-55, 1999.

[20] D. P. Myriounis, E. Z. Kordatos, S. T. Hasan and T. E. Matikas, "Crack-tip stress field and fatigue crack growth monitoring using Infrared lock-in thermography in A359/SiCp composites", *Strain,* vol. 47, pp. 619-627, 2011.

[21] B. V. Farahani, P. J. Tavares and P. M. G. P. Moreira, "SIF determination with thermoelastic stress analysis", *Procedia Structural Integrity 2,* pp. 2148-2155, 2013.

[22] F. A. Diaz, E. A. Patterson, R. A. Tomlinson and J. R. Yates, "Measuring stress intensity factors during fatigue crack growth using thermoelasticity", *Fatigue and Fracture of Engineering Materials and Structures,* vol. 27, no. 7, pp. 571-783, 2004.

[23] C. A. Middleton, A. Gaio, R. J. Greene and E. A. Patterson, "Towards automated tracking of initiation and propagation of cracks in aluminium alloy coupons using thermoelastic stress analysis", *Journal of Nondestructive Evaluation,* vol. 38, no. 18, 2019.

[24] M. Zanganeh, R. A. Tomlinson and J. R. Yates, "T-stress determination using thermoelastic stress anaylsis", *Journal of Strain Analysis for Engineering Design,* vol. 43, pp. 529-527, 2008.

[25] D. Palumbo and U. Galietti, "Thermoelastic Phase Analysis (TPA): a new method for fatigue behaviour analysis of steels", *Fatigue & Fracture of Engineering Materials & Structures,* vol. 40, pp. 523-534, 2017.

Figures

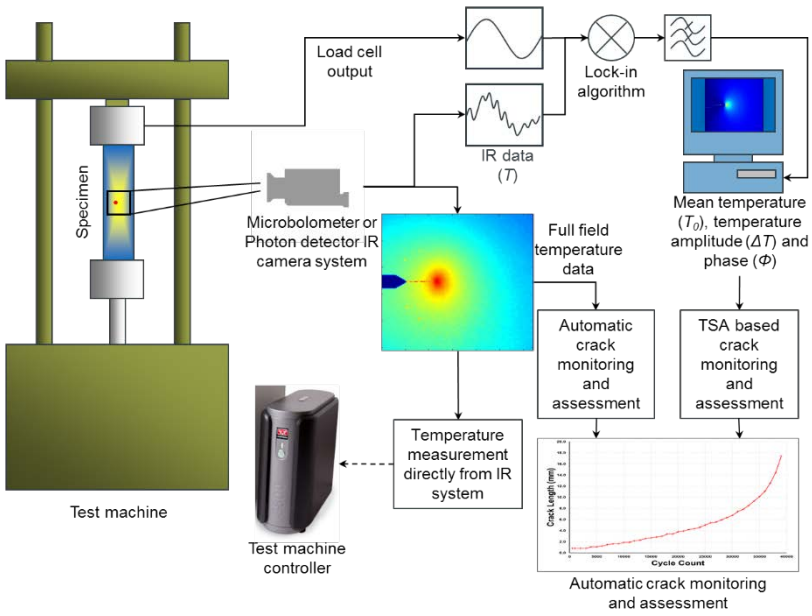

Figure 1. Proposed automatic crack monitoring and assessment procedure

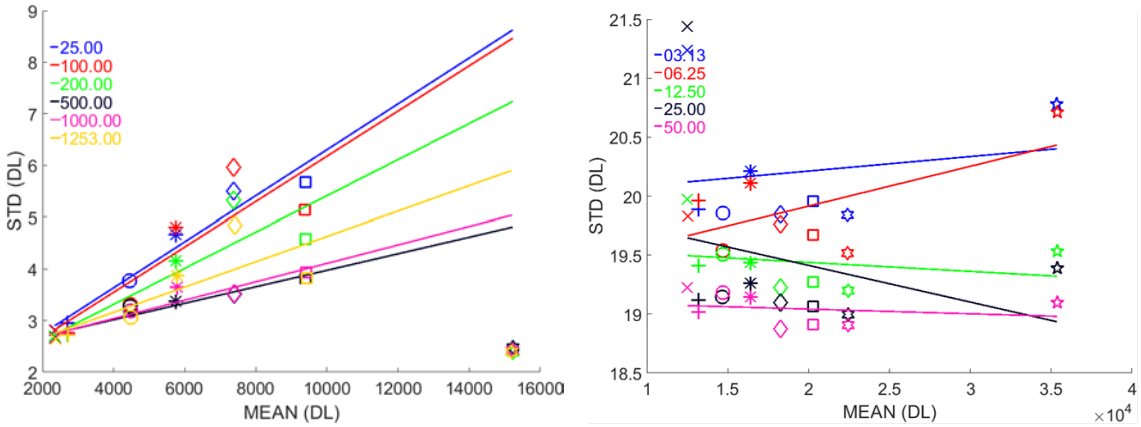

Figure 2. Noise plots for FLIR SC5500 photon detector (left) and FLIR A655SC microbolometer (right).

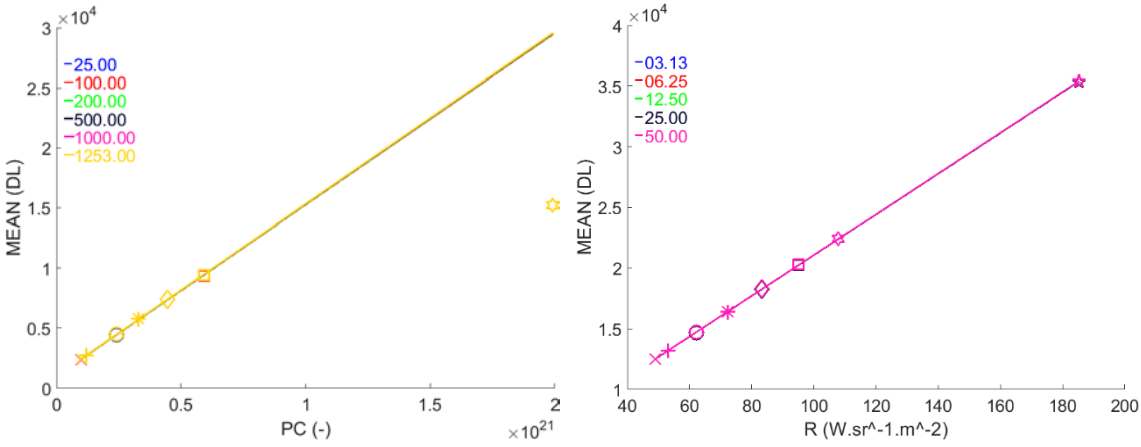

Figure 3. Sensitivity plots for FLIR SC5500 photon detector (left) and FLIR A655SC microbolometer (right).

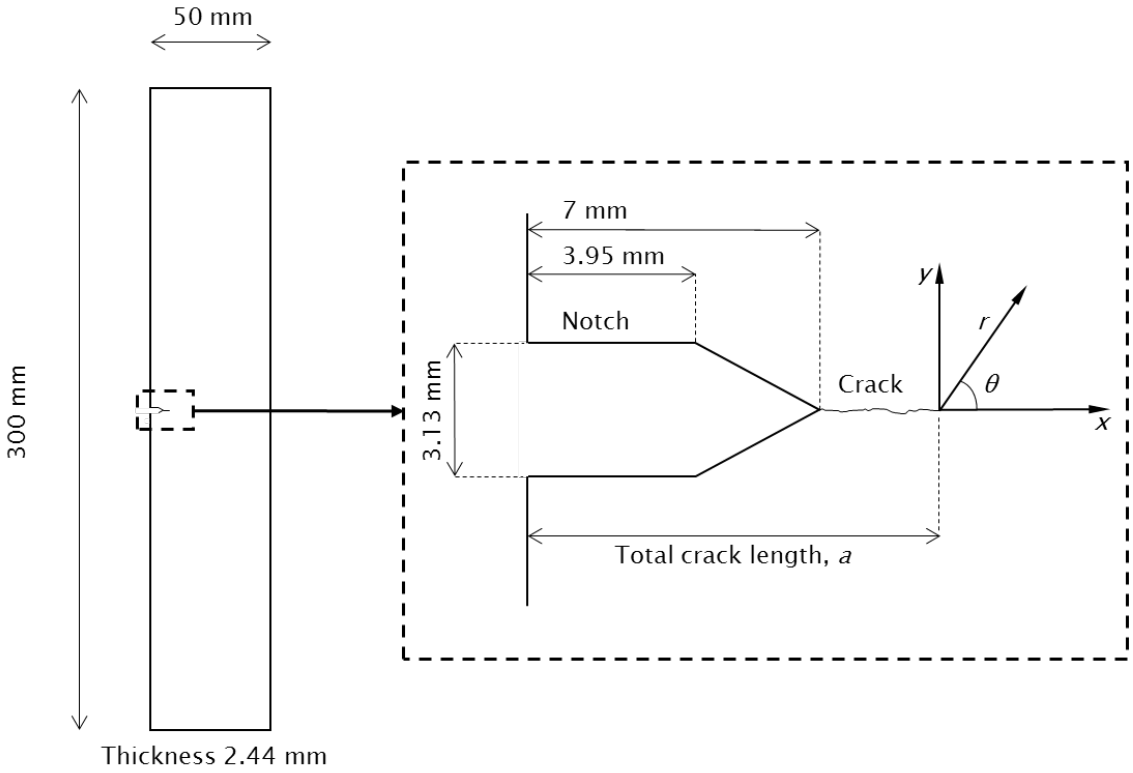

Figure 4. SENT specimen geometry and coordinate system around the crack tip

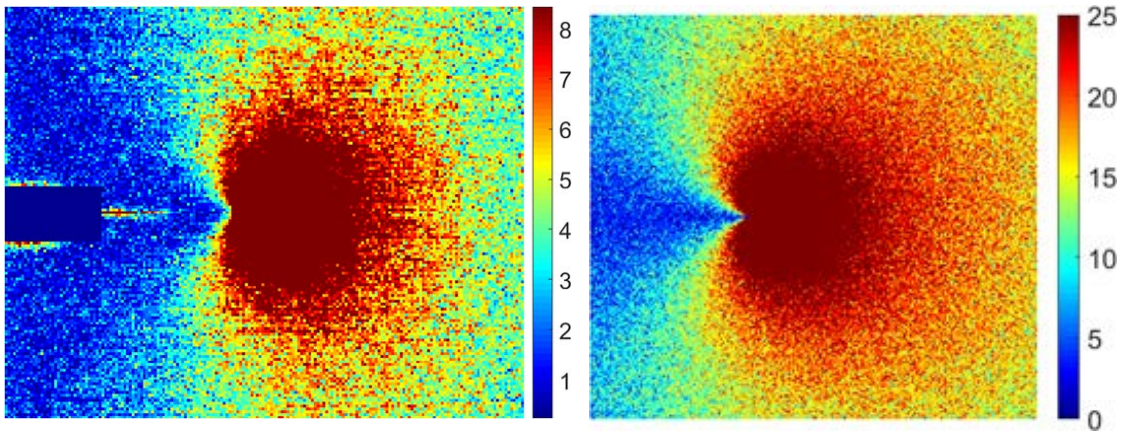

Figure 5. Thermoelastic response for microbolometer (DL), experimental (left) model (right)

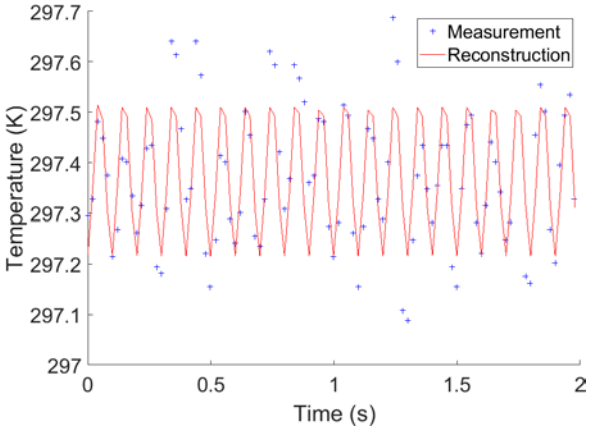

Figure 6. Response of a single pixel from the microbolometer, 5 pixels ahead of the crack tip.

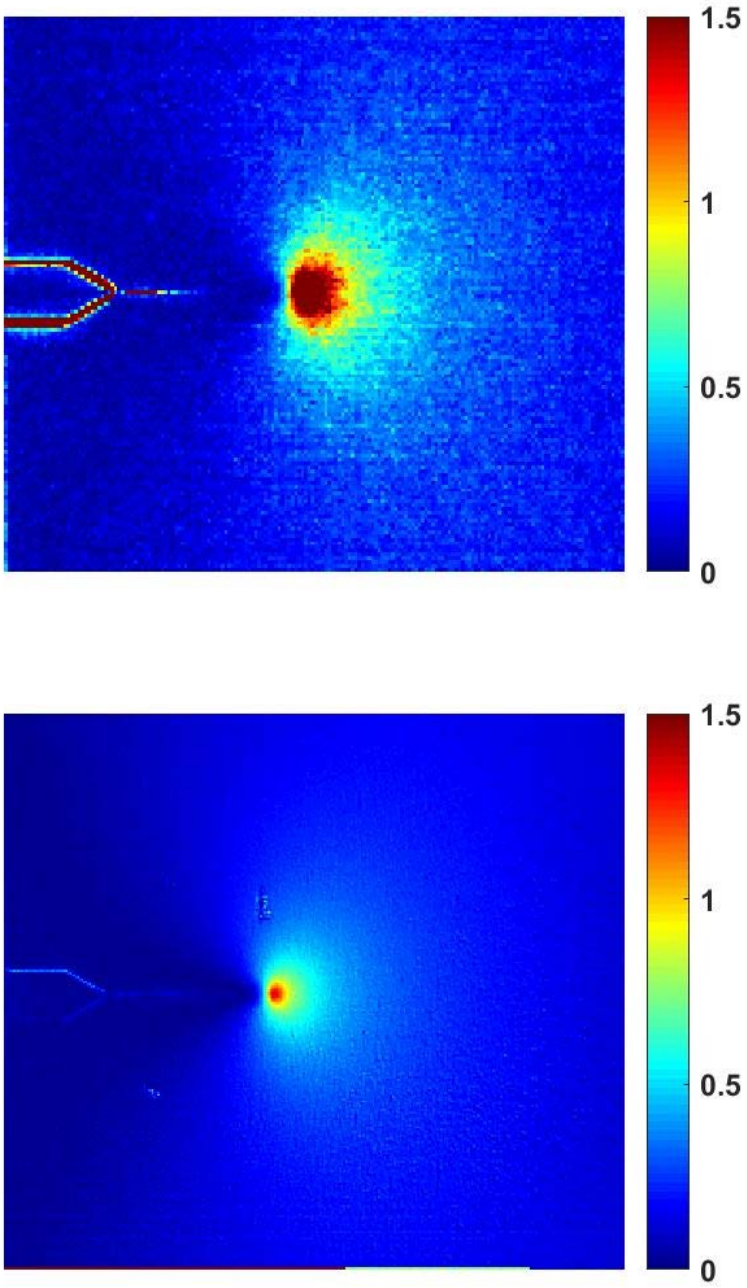

Figure 7. Microbolometer calibrated ΔT [13] (top) and photon detector measured ΔT (bottom).

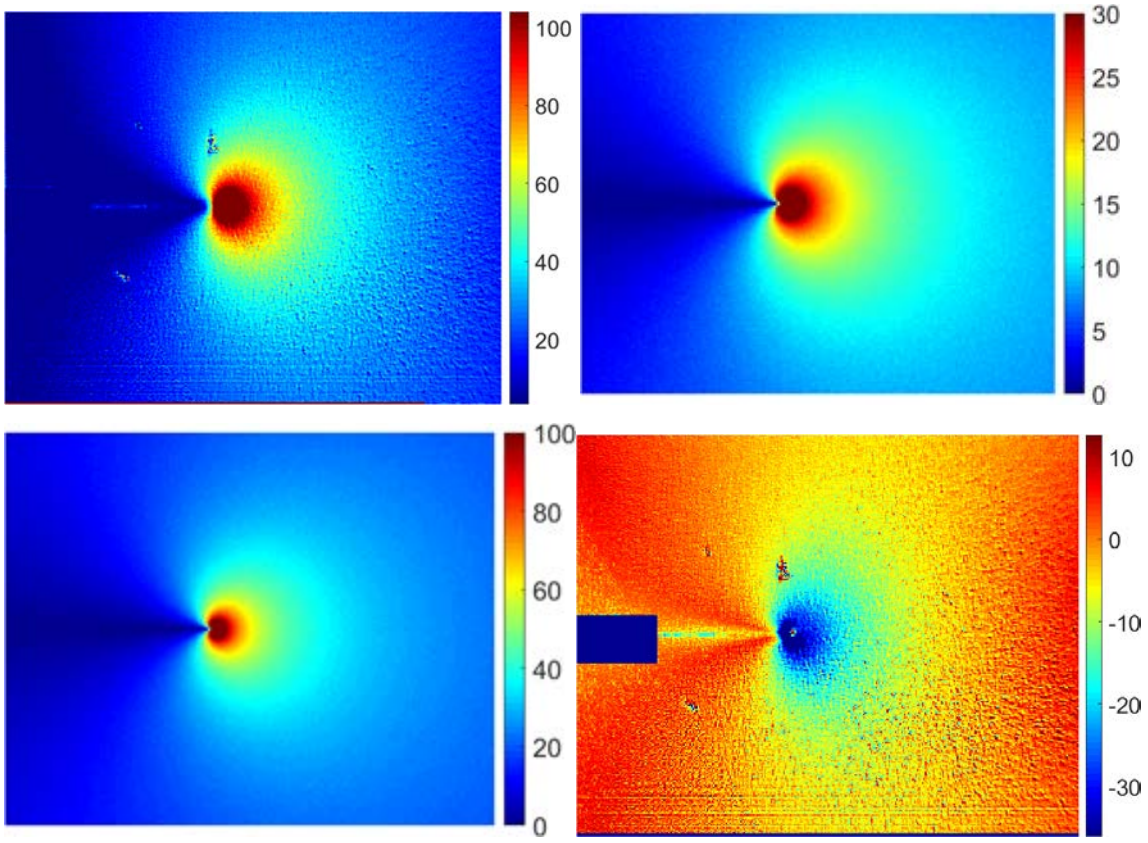

Figure 8. Thermoelastic response for photon detector (DL), experiment (top left) model IT = 500 µs (top right), model IT = 1332 µs (bottom left), Difference map of model – experiment (bottom right) IT = 1332 µs.

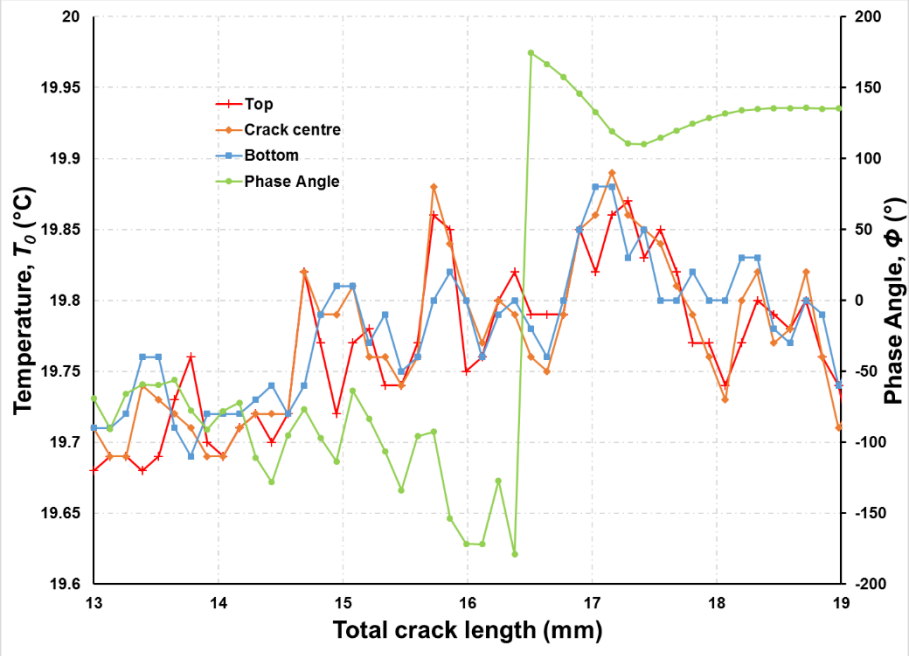

Figure 9. Typical crack profile plots of mean temperature, T_0, and phase, ϕ.

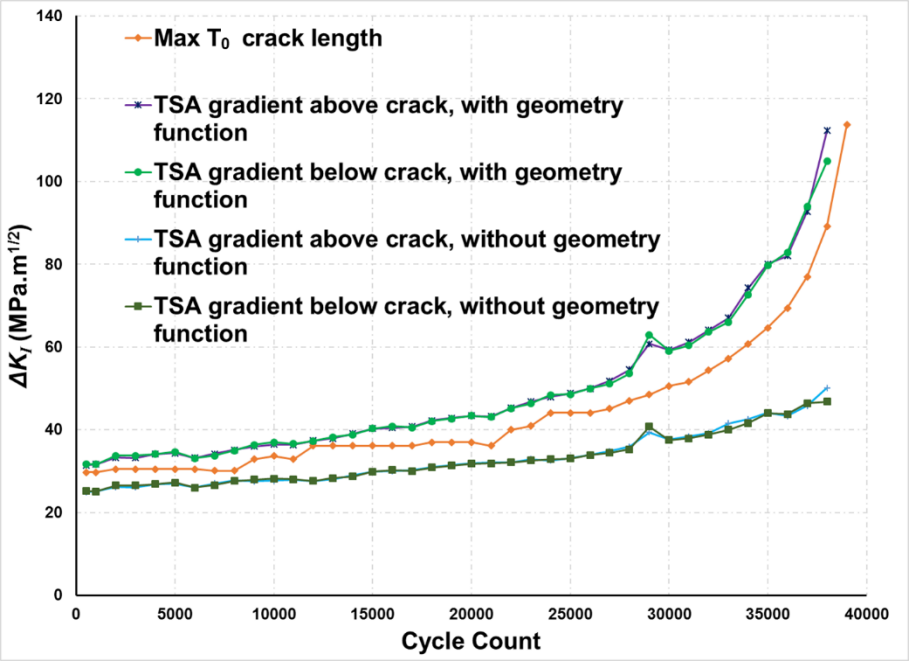

Figure 10. Evolution of ΔK_I with cycle count calculated using the maximum T_0 crack length measurement technique and from the thermoelastic response during the constant load test.

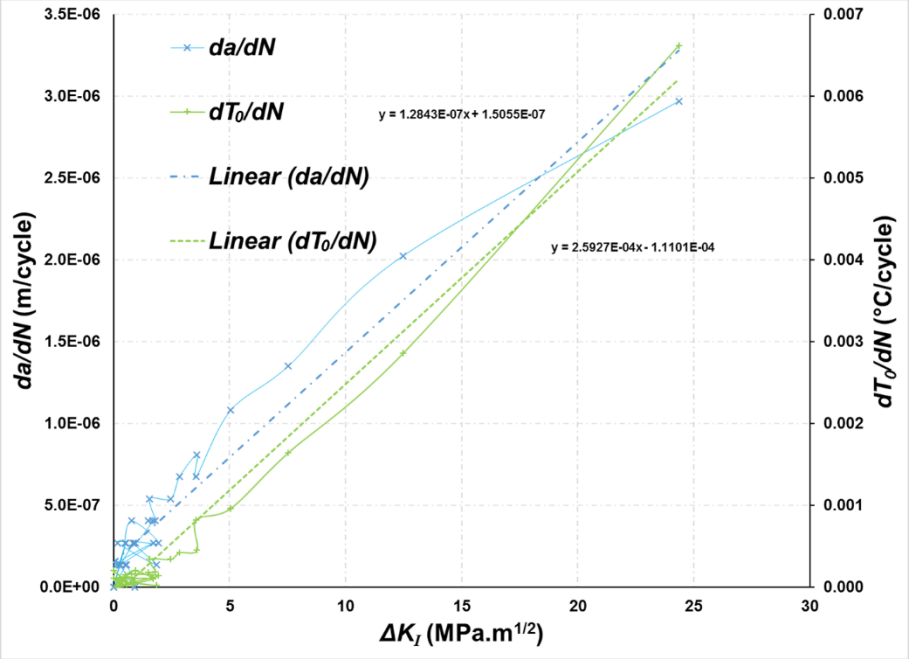

Figure 11. Plot of dT_0/dN and da/dN against ΔK_I for constant load test.

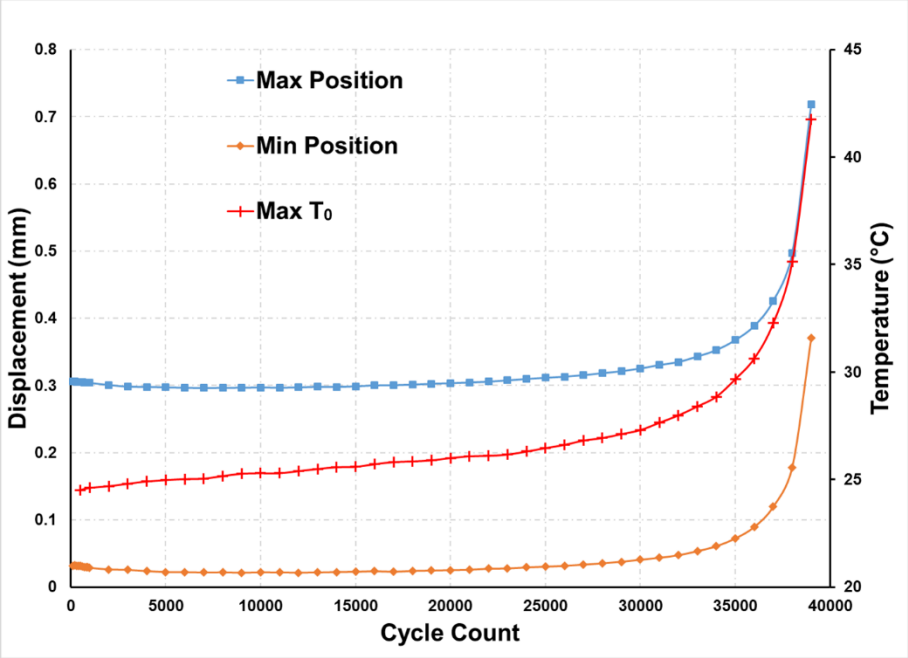

Figure 12. Evolution of the maximum temperature, T_0, and maximum and minimum position with cycle count for the constant load test.

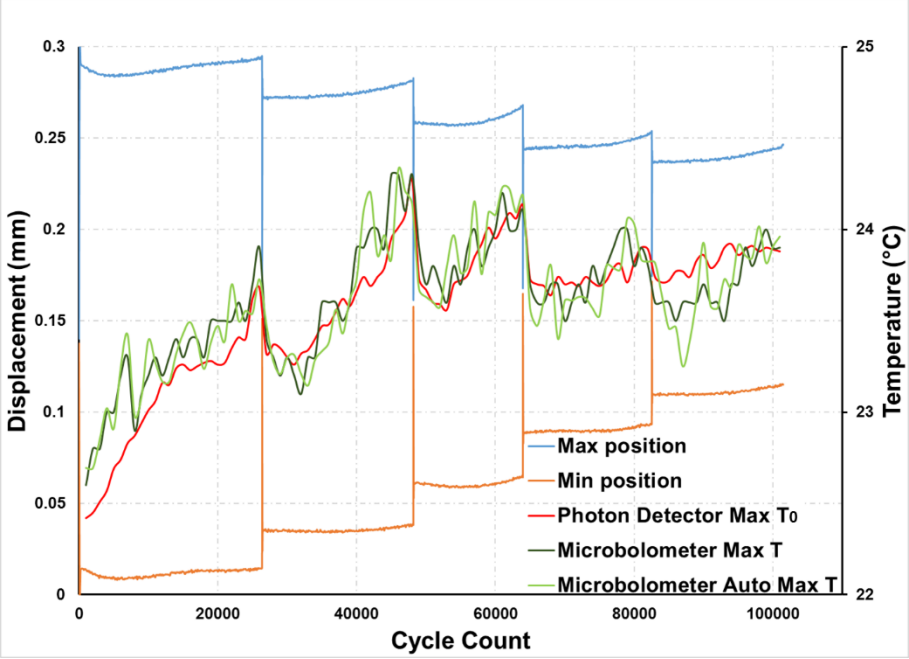

Figure 13. Evolution of the maximum temperature and maximum and minimum position with cycle count for the controlled crack growth test.

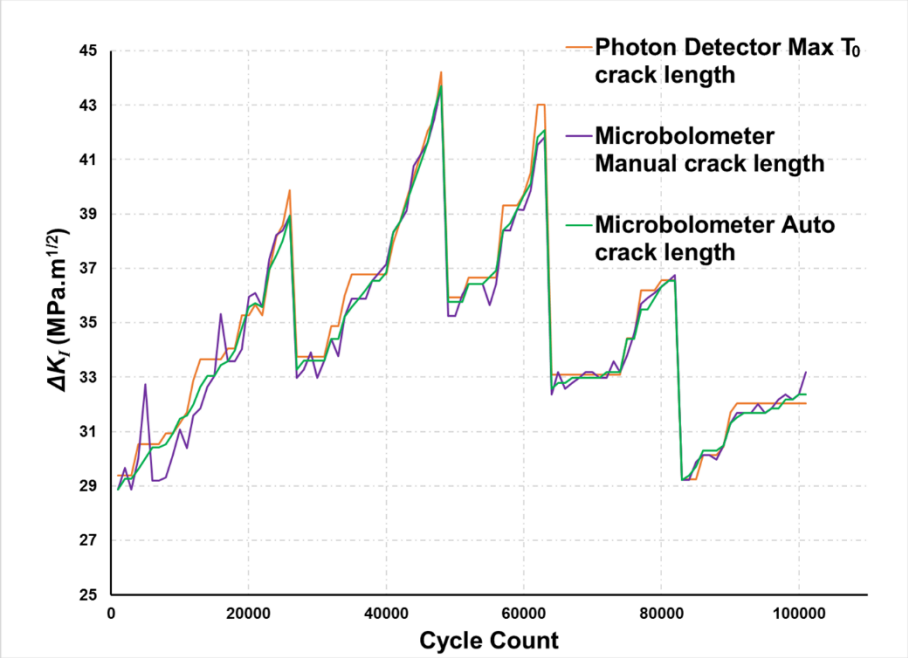

(a)

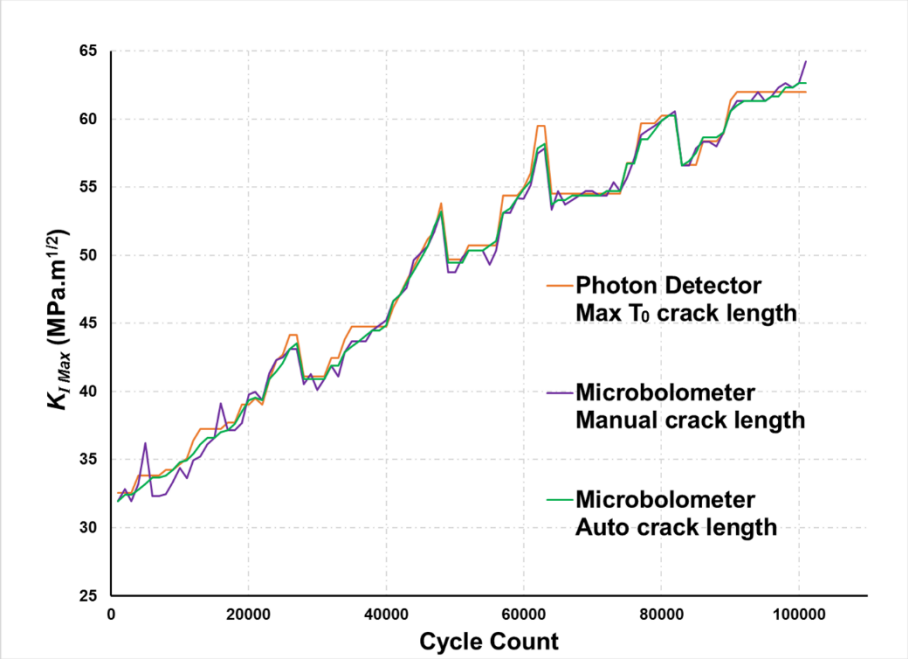

(b)

Figure 14. Evolution of SIF with cycle count calculated using the three crack length measurement techniques for the controlled crack growth test: (a) ΔK_I (b) K_{Imax}.

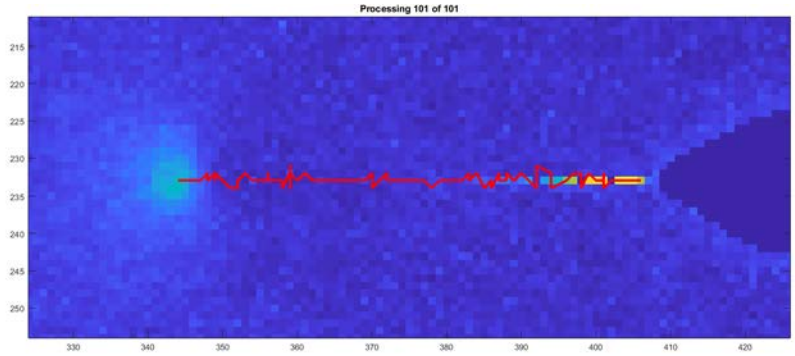

Figure 15. Screen shot from automatic crack monitoring software.